Volume 47 | Number 2 | 14 January 2018 | Pages 271–624

Dalton Transactions

An international journal of inorganic chemistry

rsc.li/dalton

ISSN 1477-9226

ROYAL SOCIETY OF CHEMISTRY

PAPER

Hongbin Liang *et al.*

Insight into Eu redox and Pr^{3+} 5d emission in $KSrPO_4$ by VRBE scheme construction

Dalton Transactions

PAPER

Cite this: *Dalton Trans.*, 2018, **47**, 306

Insight into Eu redox and Pr^{3+} 5d emission in $KSrPO_4$ by VRBE scheme construction†

Rongfu Zhou,[a] Litian Lin,[a] Chunmeng Liu,[a] Pieter Dorenbos,[b] Ye Tao,[c] Yan Huang[c] and Hongbin Liang *[a]

Received 11th October 2017,
Accepted 13th November 2017

DOI: 10.1039/c7dt03813e

rsc.li/dalton

A series of Ln-doped $KSrPO_4$ (Ln = Ce^{3+}, Eu^{3+}, Eu^{2+}, Pr^{3+}) phosphors are prepared through a high-temperature solid-state method. The $KSrPO_4$ compound is confirmed to possess a β-K_2SO_4 structure with the *Pnma* group by Rietveld refinement, and the temperature-dependent lattice parameters are investigated with the powder X-ray diffraction results at different temperatures. Ce^{3+} and Eu^{3+} ions are introduced to probe the crystal field strength (CFS) and the lanthanide site symmetry by using VUV-UV-vis spectroscopy. The temperature-dependent luminescence properties of $KSrPO_4$: Ce^{3+}/Eu^{2+} exhibit an excellent thermal stability of Ce^{3+}/Eu^{2+} luminescence. Based on the VUV-UV-vis spectra of Ce^{3+} and Eu^{3+} doped $KSrPO_4$, the vacuum referred binding energy (VRBE) scheme is constructed to understand the redox properties of Eu, the 5d energy levels of Pr^{3+} and the thermal quenching characteristics of Ce^{3+} and Eu^{2+} luminescence.

1. Introduction

Eu^{2+}-Activated luminescence materials have drawn wide attention because of their importance in solid-state lighting and displays.[1–4] The preparation of divalent europium doped materials often needs reducing conditions, for example, a H_2 or CO ambiance, *etc*. But in some special cases, Eu^{2+} can also be (partially) obtained through a solid-state reaction approach with Eu(III)-containing raw materials under non-reducing conditions.[5,6] This is, of course, the result of composition and structure of these special host compounds. From the viewpoint of electron transfer, the redox processes of Eu^{3+} and Eu^{2+} as dopants in solid state inorganic compounds relate to factors such as the electronic structure of the conduction band and valence band, the band gap energy and the Fermi level of the host compound, the 5d energy of Eu^{2+}, and the energy of charge transfer state (CTS) between Eu^{3+} and coordinated atoms.[7] A clear understanding of the redox behaviour of Eu^{2+}/Eu^{3+} in different host compounds is a key issue for the preparation and application of Eu^{2+}-activated luminescence materials.

Eu^{2+}, Pr^{3+} and Ce^{3+} doped luminescence materials are also applied as important scintillators. SrI_2: Eu^{2+}, and LnX_3: Ce^{3+} (Ln = La, Lu; X = Br, I) are commercially available scintillators in various detecting areas.[8–10] These applications are benefited from the typical parity-allowed 5d–4f transitions of these ions and therefore with fast radiative rates. In the same site of the same host compound, fluorescence decay of Pr^{3+} is usually faster than that of Ce^{3+} or Eu^{2+} due to its shorter emission wavelength.[11] Therefore, Pr^{3+} is an important activator in fast decay scintillators. Because the binding energy of outer 5d electrons is highly sensitive to the local coordination environment of the host lattice, it is essential to fully understand the energy and thermal stability of d–f emission of Pr^{3+} in various host compounds to find novel Pr^{3+} doped scintillation materials.

The compound $KSrPO_4$ is one of the $ABPO_4$ (A = monovalent cations, B = divalent cations) monophosphates with tetrahedral rigid anion groups.[12] And Eu^{2+}, Tb^{3+}, $Sm^{2+/3+}$ doped $KSrPO_4$ phosphors exhibit excellent luminescence properties.[13–15] In this paper, we investigate the temperature- and doping concentration- dependent synchrotron radiation VUV-UV-vis luminescence spectra of Ce^{3+}, Pr^{3+}, Eu^{3+} and Eu^{2+} doped $KSrPO_4$. In particular, the electronic scheme with the vacuum referred binding energies (VRBE) for all lanthanide ions is constructed based on the measured band gap energy, 5d orbital energies of Ce^{3+} and Eu^{3+}–O^{2-} charge transfer energy with the purpose to understand the excellent thermal stabilities of luminescence of Ce^{3+} and Eu^{2+}, the 5d energies of Pr^{3+} and the redox of Eu. Eu-doped samples are prepared in inert N_2, oxidizing air and under reducing CO conditions to gain clearer insight into the redox characteristics of Eu in

[a]*MOE Key Laboratory of Bioinorganic and Synthetic Chemistry, KLGHEI of Environment and Energy Chemistry, School of Chemistry, Sun Yat-sen University, Guangzhou 510275, China. E-mail: cesbin@mail.sysu.edu.cn; Tel: +86 20 84113695*
[b]*Faculty of Applied Sciences, Delft University of Technology, Mekelweg 15, 2629 JB Delft, The Netherlands*
[c]*Beijing Synchrotron Radiation Facility, Institute of High Energy Physics, Chinese Academy of Sciences, Beijing 100039, China*

†Electronic supplementary information (ESI) available. See DOI: 10.1039/c7dt03813e

$KSrPO_4$. This work demonstrates a convenient approach to predict the stability of dopant Eu^{2+}/Eu^{3+} and the energy of d–f emission of Pr^{3+} in a specific host compound.

2. Experimental

Ln-doped $KSrPO_4$ (Ln = Ce^{3+}, Eu^{3+}, Eu^{2+}, Pr^{3+}) samples are prepared using a conventional solid-state reaction route. The analytical grade reagents $SrCO_3$, K_2CO_3, $NH_4H_2PO_4$ and 99.99% pure rare-earth oxides Eu_2O_3, CeO_2, Pr_6O_{11} are used as starting materials. These reactants are thoroughly ground in an agate mortar and pre-fired at 975 K under an air atmosphere for 5 h. Then Ce^{3+} or Pr^{3+} doped samples are annealed at 1570 K for 3 h in a CO ambiance which are produced from the incomplete combustion of carbon at high-temperature. Europium doped sample batches with each at a specific concentration are divided into three parts and fired in reducing CO, inert N_2, or oxidizing air flow, respectively. Finally, the samples are cooled to RT by switching off the muffle furnace and ground into powder for subsequent analysis.

The phase purity of the samples is estimated by powder X-ray diffraction (P-XRD) on a Bruker D8 advanced X-ray diffractometer with a wavelength of 1.54056 Å Cu Kα radiation at 40 kV and 40 mA, demonstrating no detectable impurity phase in all samples. High quality P-XRD data for the refinement are collected within the 2θ range from 7° to 110° at a 2θ step of 0.02°. The Rietveld refinement is performed using the TOPAS – Academic program.[16]

The UV-vis excitation and emission spectra as well as the luminescence decay curves are recorded with an Edinburgh FLS 920 combined fluorescence lifetime and steady-state spectrometer equipped with a thermo-electronic cooled (−19.5 °C) Hamamatsu R928P Model photomultiplier. The 450 W xenon lamp is used as the excitation source of steady-state excitation and corresponding emission spectra. A 150 W nF900 lamp with a pulse width of 1 ns and a 60 W μF flash lamp with a pulse width of 1.5–3.0 μs are used for the measurements of decay curves. The temperature dependent spectral measurements at 77–500 K range are performed by putting the samples in a liquid nitrogen cooling OptistatDN2 cryostat and controlled by using an Oxford MercuryiTC temperature controller. The excitation and emission spectra in the VUV-UV range are obtained on the beam line 4B8 of the Beijing Synchrotron Radiation Facility (BSRF) under normal operating conditions using the spectrum of sodium salicylate (o-$C_6H_4OHCOONa$) as a standard.[11,17]

3. Results and discussion

3.1. Structure and phase characterization

Fig. 1 shows the Rietveld refinement results based on the laboratory P-XRD data of the synthesized $KSrPO_4$ compound

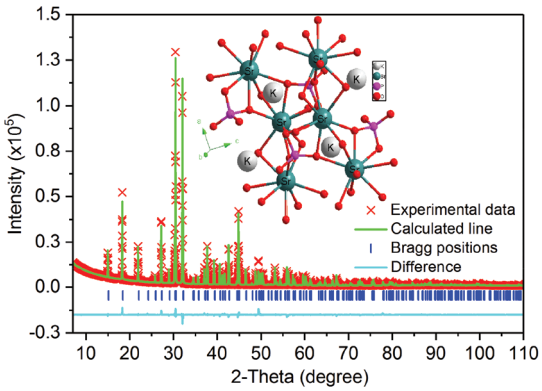

Fig. 1 Experimental (red crosses) and calculated (green solid line) XRD patterns, their difference (cyan solid line), and the Bragg reflection positions (blue ticks) of $KSrPO_4$; the inset shows the crystal structure of $KSrPO_4$.

using the *Pnma* structure model.[18,19] No impurity peak is observed, and the obtained reliability factors R_{wp}, R_p and R_B are 5.89%, 3.57%, and 5.92%, respectively. The final refined structural parameters are listed in ESI Table S1.† The $KSrPO_4$ compound is crystallized in an orthorhombic structure with the space group *Pnma*. The lattice parameters are a = 7.34706(4) Å, b = 5.55249(3) Å, c = 9.61716(6) Å and V = 392.325(4) Å^3. The inset of Fig. 1 depicts the crystal structure of $KSrPO_4$. A Sr^{2+} atom is coordinated by nine oxygen atoms with C_s point symmetry. The average bond length between Sr^{2+} and O^{2-} is ~2.688 Å (ESI Table S2†) and the nearest distance of two adjacent Sr^{2+} ions is ~3.809 Å. The polyhedral SrO_9, KO_{10} and PO_4 form the framework of the $KSrPO_4$ structure by sharing their corner or edges. ESI Fig. S1† shows the representative P-XRD patterns of Ce^{3+}, Eu^{3+}, Pr^{3+} and Eu^{2+} singly doped $KSrPO_4$ samples. All XRD patterns are in good agreement with the refined $KSrPO_4$ result, implying that all samples are of a single pure phase and the doping of $Ce^{3+}/Eu^{3+}/Pr^{3+}/Eu^{2+}$ ions does not significantly influence the diffractogram of the host compound. Due to the more suitable ionic size and valence state [$r(Ce^{3+})$ = 1.336 Å, $r(Eu^{3+})$ = 1.26 Å, $r(Pr^{3+})$ = 1.319 Å, $r(Eu^{2+})$ = 1.44 Å, $r(Sr^{2+})$ = 1.45 Å; coordination number = 9],[20] Ce^{3+}, Eu^{3+}, Pr^{3+} and Eu^{2+} may prefer occupying the Sr^{2+} site when doped into $KSrPO_4$.

To study the thermal evolution of the host structure, Fig. 2(a) displays the P-XRD patterns of $KSrPO_4$ at temperatures from 223 to 523 K. $KSrPO_4$ maintains the orthorhombic structure (space group *Pnma*) in the investigated temperature range. The magnified patterns from 31.9 to 32.2 degree of 2-theta in Fig. 2(b) show that the diffraction peaks slightly shift to the lower angle side, which implies that the unit cell of the host undergoes a thermal expansion. Based on these XRD patterns, the lattice constants can be calculated by Rietveld refinement. As displayed in Fig. 2(c), the lattice parameters a, b, c and V are found to increase with rising temperature, which may affect the luminescence properties of the samples as discussed later.

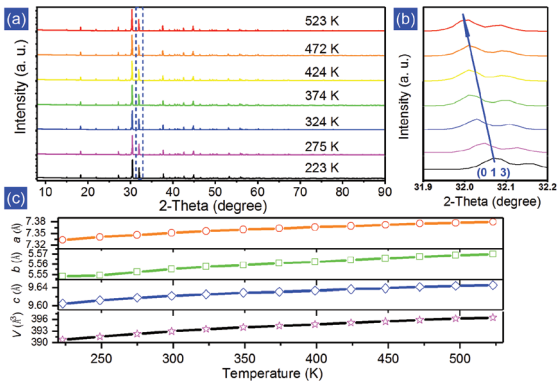

Fig. 2 (a) Temperature-dependent P-XRD patterns of $KSrPO_4$ in the temperature range of 223–523 K; (b) magnified P-XRD patterns (31.9–32.2 degree of 2-theta) of $KSrPO_4$; (c) lattice parameters *a*, *b*, *c* and *V* of $KSrPO_4$ as a function of temperature.

3.2. Luminescence of Ce^{3+} in $KSrPO_4$

Fig. 3 shows the VUV-UV excitation (λ_{em} = 332 nm) spectrum of the sample with the nominal composition $K_{1.001}Sr_{0.998}Ce_{0.001}PO_4$ at 25 K. The high-lying excitation band with a maximum at about 7.65 eV (band H) is attributed to the excitonic absorption of the $KSrPO_4$ host. The absorptions below ~6.50 eV are assigned to the f–d excitation bands of Ce^{3+} in $KSrPO_4$. In this range, three clear bands A, C, and D can be observed. The bands A and D have shoulder bands B and E at their higher energy sides, respectively. When we assume that Ce^{3+} ions occupy nine-fold coordinated Sr^{2+} sites with a low symmetry C_s group, the 5d orbitals of Ce^{3+} should be split into five non-degenerate orbitals. Therefore, the excitation curve in the 3.87–6.55 eV (190–320 nm) spectral range is fitted by a sum of five Gaussian functions to estimate the energies of 4f–5d transitions of Ce^{3+}. These energies are at about 4.14 (A), 4.60 (B), 5.23 (C), 5.76 (D), and 6.08 (E) eV, respectively. Consequently, the centroid energy of Ce^{3+} 5d states, *viz.* the arithmetic mean energy of the five f–d excitation bands, is calculated to be about 5.16 eV, meaning that the down-shift of the centroid energy of the Ce^{3+} 5d state (ε_c) in $KSrPO_4$ is about 1.19 eV with respect to that of free gaseous Ce^{3+} (6.35 eV). This value is near those of other phosphates, such as $K_3Lu(PO_4)_2$ (1.17 eV),[21] YPO_4 (1.19 eV),[21] $Ca_9Y(PO_4)_7$ (1.20 eV),[22] and $LuPO_4$ (1.20 eV),[21] which implies that Ce^{3+} ions in these phosphate compounds have nearly the same nephelauxetic effect, covalence or spectroscopic polarization.[21,23] Meanwhile, the experimental crystal field splitting of Ce^{3+} in $KSrPO_4$ is calculated to be approximately 1.94 eV by subtracting the energy of the first 5d orbital (4.14 eV) from that of the fifth 5d one (6.08 eV). This value is in the range of those of Ce^{3+} in compounds SrB_4O_7 (1.66 eV),[24] $Sr_2Mg(BO_3)_2$ (2.10 eV),[25] and $SrAl_2O_4$ (2.68 eV, 2.75 eV),[26] in which Ce^{3+} ions occupy nine-fold Sr^{2+} sites with C_s or C_1 symmetry.

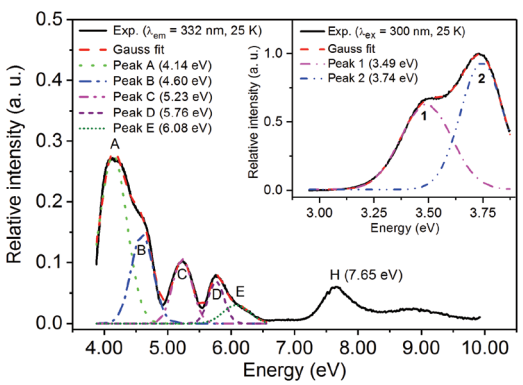

Fig. 3 Synchrotron radiation VUV-UV excitation (λ_{em} = 332 nm) spectrum of $K_{1.001}Sr_{0.998}Ce_{0.001}PO_4$ at 25 K and the corresponding Gaussian fitting results; the inset shows the emission (λ_{ex} = 300 nm) spectrum at 25 K and the fitting results.

The emission (λ_{ex} = 300 nm) spectrum of $K_{1.001}Sr_{0.998}Ce_{0.001}PO_4$ at 25 K is fitted using a sum of two Gaussian components as displayed in the inset of Fig. 3. The obtained two bands (1, ~3.49 eV; 2, ~3.74 eV) originated from the transitions from the lowest 5d state to its ^2F_J (J = 7/2, 5/2) 4f ground state of Ce^{3+}, respectively. Their energy difference is evaluated to be about 0.25 eV (2.02×10^3 cm^{-1}), which is coincident with the theoretical energy difference of ^2F_J (J = 5/2, 7/2) multiplets (~2.00×10^3 cm^{-1}). According to the energy difference between the band peaks of the lowest 5d and $^2F_{5/2}$ transition in excitation and emission spectra, the Stokes shift of Ce^{3+} is approximately 0.40 eV (~3.23×10^3 cm^{-1}). The Stokes shift is related to the Huang–Rhys parameter and effective phonon energy and depends on the characteristic of the material. The value in the present case is close to that in other monophosphates, such as $NaCaPO_4$ (0.38 eV), and $LiSrPO_4$ (0.40 eV).[27,28] ESI Fig. S2† shows the highest-height normalized VUV-UV excitation (λ_{em} = 332 and 354 nm) and emission (λ_{ex} = 200, 215, 235, 270 and 300 nm) spectra of sample $K_{1.001}Sr_{0.998}Ce_{0.001}PO_4$ at 25 K. The excitation spectra by monitoring different emission wavelengths overlap with each other, and the emission spectra at different excitation wavelengths also have similar profiles. These phenomena demonstrate that the sample is without the impurity phase and reveal the occurrence of only one kind of Ce^{3+} luminescence center in the sample as we mentioned above. In ESI Fig. S3†, the luminescence decay curves at different wavelengths further confirm this result. They all possess the same exponential decay properties and the lifetime of Ce^{3+} in $KSrPO_4$ is evaluated to be about 25.7 ns.

The height-normalized excitation (λ_{em} = 375 nm) and emission (λ_{ex} = 270 nm) spectra of samples $K_{1+x}Sr_{1-2x}Ce_xPO_4$ (x = 0.001, 0.003, 0.009, 0.019 and 0.03) are plotted in Fig. 4. With increasing Ce^{3+} content, the excitation bands of the 4f–$5d_1$ transition and emission spectra gradually shift to lower energies, and the intensity of $5d_1$–$^2F_{7/2}$ emission increases with respect to that of $5d_1$–$^2F_{5/2}$. Since smaller Ce^{3+} ions occupy larger Sr^{2+} sites, the lattice may experience a little contraction and the CFS around Ce^{3+} becomes larger, which pushes the $5d_1$ level towards lower energies. The zero phonon line (ZPL)

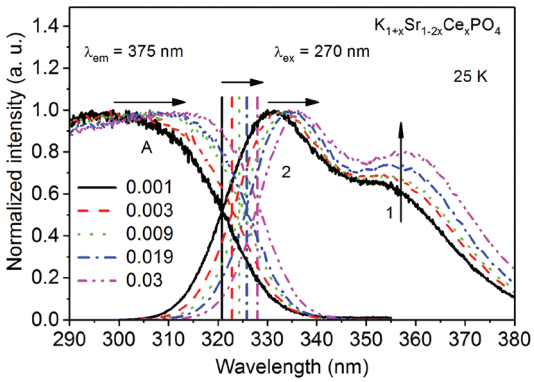

Fig. 4 Height-normalized excitation (λ_{em} = 375 nm) and emission (λ_{ex} = 270 nm) spectra of samples $K_{1+x}Sr_{1-2x}Ce_xPO_4$ (x = 0.001, 0.003, 0.009, 0.019 and 0.03) in the 290–380 nm range at 25 K.

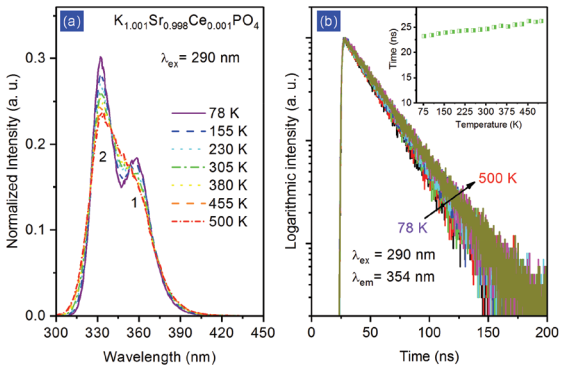

Fig. 5 (a) Normalized emission (λ_{ex} = 290 nm) spectra and (b) decay curves (λ_{ex} = 290 nm, λ_{em} = 354 nm) of Ce^{3+} in $K_{1.001}Sr_{0.998}Ce_{0.001}PO_4$ at different temperatures; the inset of (b) represents the temperature-dependent decay times of Ce^{3+}.

position directly indicates the energy of the 4f–5d$_1$ transition of Ce^{3+}. Its position can be estimated as the intersection point of the excitation and emission spectra, although we did not observe ZPLs in the spectra.[29] Fig. 4 shows the red shift of the intersection point with increasing Ce^{3+} doping, indicating that ZPLs shift to lower energies with stronger CFS around Ce^{3+}. Accordingly, the emission peaks of Ce^{3+} gradually shift to longer wavelengths. Moreover, in consideration of the significant overlap between the excitation and emission spectra, the self-absorption effect of Ce^{3+} is also active in our case. This effect also shifts the emission band to the lower energy side to some extent, and meanwhile gives rise to the decrease of the relative intensity of 5d$_1$–^{2}F$_{5/2}$ emission.[11,29] Therefore, the relative intensity of 5d$_1$–^{2}F$_{7/2}$ emission looks stronger in the height-normalized spectra. ESI Fig. S4(a)† shows the concentration-dependent emission spectra of $K_{1+x}Sr_{1-2x}Ce_xPO_4$ (x = 0.001, 0.003, 0.009, 0.019 and 0.03) samples under 270 nm excitation at RT. With the increase of doping contents, the emission intensities of Ce^{3+} increase gradually, demonstrating that concentration quenching does not occur in this concentration range. The luminescence decay curves (λ_{ex} = 290 nm, λ_{em} = 354 nm) of samples are shown in ESI Fig. S4(b).† All curves follow the exponential characteristic and overlapped with each other, further confirming that the concentration quenching of Ce^{3+} emission does not occur until x = 0.03.

Fig. 5 displays the normalized emission (λ_{ex} = 290 nm) spectra and the decay curves (λ_{ex} = 290 nm, λ_{em} = 354 nm) of sample $K_{1.001}Sr_{0.998}Ce_{0.001}PO_4$ at different temperatures. From 78 to 500 K, the emission band shows a bit of short-wavelength shift, because of the lattice expansion resulting from the weaker crystal field strength at higher temperatures. Moreover, the intensities of Ce^{3+} 5d$_1$–^{2}F$_J$ (J = 5/2, 7/2) transitions decrease gradually, and the high-energy 5d$_1$–^{2}F$_{5/2}$ emission reduces relatively faster than the low-energy 5d$_1$–^{2}F$_{7/2}$ as seen in Fig. 5(a). This is due to the enhanced reabsorption at higher temperatures as illustrated in ESI Fig. S5.† Meanwhile, two partial-resolved emissions become more overlapped because of the thermal-broadening of both bands. All decay curves in Fig. 5(b) show exponential properties and no shortening lifetime with rising temperature, implying that the thermal quenching of Ce^{3+} emission does not occur yet. Instead, the slight increase of Ce^{3+} decay time can be observed in the inset of Fig. 5(b). In consideration of the self-absorption at higher temperature, the lifetime of Ce^{3+} can be slightly lengthened.[30]

3.3. Luminescence of Eu^{3+} in $KSrPO_4$ and construction of the VRBE scheme

Fig. 6 displays the synchrotron radiation VUV-UV excitation spectrum (a, λ_{em} = 610 nm) and the laboratory UV-vis excitation spectrum (b, λ_{em} = 611 nm) of the $K_{1.003}Sr_{0.994}Eu_{0.003}PO_4$ sample at RT. The peak position and band shape of the high energy excitation band (162 nm, 7.65 eV) are the same as that in Fig. 3, and this band definitely corresponds to the excitonic absorption of this phosphate host. For the electron and hole binding energy in the exciton, we will assume a value of 0.008 $(E^{ex})^2$ as proposed in ref. 31. Accordingly, the bottom of the conduction band is estimated to be about 7.65 + 0.47 = 8.12 eV higher than the top of the valence band. The intense broad excitation band at about 272 nm (4.56 eV) is assigned to the

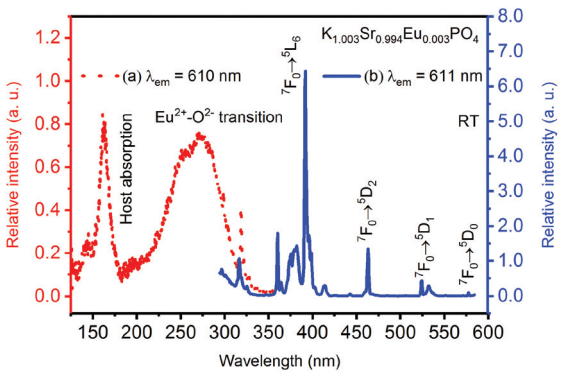

Fig. 6 Synchrotron radiation VUV-UV excitation spectrum (a, λ_{em} = 610 nm) and the laboratory UV-vis excitation spectrum (b, λ_{em} = 611 nm) of the $K_{1.003}Sr_{0.994}Eu_{0.003}PO_4$ sample at RT.

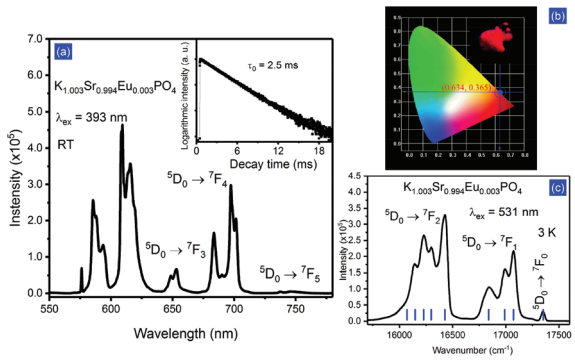

Fig. 7 (a) Emission spectrum (λ_{ex} = 393 nm) of the $K_{1.003}Sr_{0.994}Eu_{0.003}PO_4$ sample at RT. The inset shows the decay curve (λ_{ex} = 393 nm, λ_{em} = 611 nm) of Eu^{3+} in $K_{1.003}Sr_{0.994}Eu_{0.003}PO_4$; (b) CIE chromaticity diagram for $K_{1.003}Sr_{0.994}Eu_{0.003}PO_4$ excited at 393 nm, the inset shows the digital photograph of $K_{1.003}Sr_{0.994}Eu_{0.003}PO_4$ upon 365 nm UV lamp excitation; (c) detailed emission spectrum (λ_{ex} = 531 nm) of the $K_{1.003}Sr_{0.994}Eu_{0.003}PO_4$ sample at 3 K.

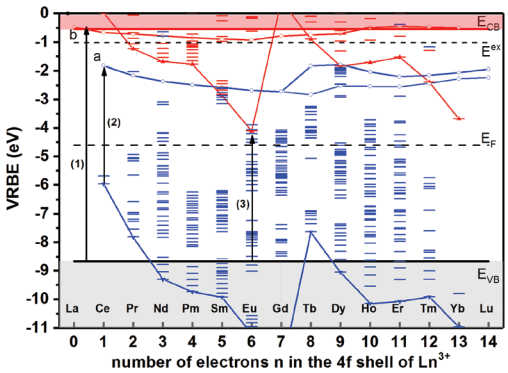

Fig. 8 Vacuum referred binding energy scheme for all lanthanide 4f (bar) and 5d (circle) states in $KSrPO_4$. Curve a connects the lowest 5d state of the trivalent lanthanide and curve b that of the lowest 5d state of the divalent lanthanide.

Eu^{3+}–O^{2-} charge transfer transition. A series of sharp lines due to the f–f transition of Eu^{3+} can be observed below 300 nm.

Fig. 7(a) shows the emission spectrum (λ_{ex} = 393 nm) of $K_{1.003}Sr_{0.994}Eu_{0.003}PO_4$ at RT, which contains a series of 4f intra-configurational transitions from the excited $^5D_0$ level to ^7F_J (J = 0, 1, 2, 3, 4 and 5), and the strongest emission is the $^5D_0$–$^7F_2$ transition with a maximum at 609.3 nm. The emission intensity of the $^5D_0$–$^7F_2$ transition is hypersensitive to the Eu^{3+} micro-environment and depends closely on the point symmetry of the Eu^{3+} site. The occurrence of the dominant $^5D_0$–$^7F_2$ transition indicates that the Eu^{3+} ion is incorporated into a site without inversion symmetry. The main $^5D_0$–$^7F_2$ transition together with the strong $^5D_0$–$^7F_4$ transition results in the deep-red luminescence of the $K_{1.003}Sr_{0.994}Eu_{0.003}PO_4$ phosphor with CIE chromaticity coordinates (0.634, 0.365) as shown in Fig. 7(b). Meanwhile, the lifetime is found to be 2.5 ms as shown in the inset of Fig. 7(a).

Provided that Eu^{3+} ions occupy the Sr^{2+} sites with C_s point symmetry, the degeneracy of each $^7F_{0,1,2}$ multiplet of Eu^{3+} would be completely lifted. To verify the site symmetry of Eu^{3+} in $KSrPO_4$, in Fig. 7(c) we give a more detailed emission spectrum of sample $K_{1.003}Sr_{0.994}Eu_{0.003}PO_4$ in the 15 750–17 500 cm^{-1} range, which is measured with step size 0.05 nm under the 531 nm $^7F_0$–$^5D_1$ transition excitation at 3 K. Since the $^5D_0$–$^7F_0$ transition will not be split, it can be used to determine the number of sites occupied. The single weak sharp line at 17 350 cm^{-1} of the $^5D_0$–$^7F_0$ transition confirms one specific Eu^{3+} site occupation in $KSrPO_4$. Three emission lines in the 16 715–17 160 cm^{-1} range are the results of magnetic-dipole $^5D_0$–$^7F_1$ transitions, and the lines in the range from 15 850 to 16 550 cm^{-1} are ascribed to the electric-dipole $^5D_0$–$^7F_2$ transitions. The $^5D_0$–$^7F_2$ emission splits into four clear lines and one line trailing in the low wavenumber side, in agreement with the substitution of Sr^{2+} sites with C_s point symmetry. In addition, it is reported that the intensity ratio of $^5D_0$–$^7F_0$ transition to $^5D_0$–$^7F_2$ transition commonly gives information on the magnitude of the J-mixing effect associated with the $^5D_0$–$^7F_0$ transition.[32] The very small ratio (0.013) in the present case suggests that the J-mixing effect can be neglected.

Fig. 8 displays the vacuum referred binding energy (VRBE) scheme for all lanthanide 4f and 5d states in $KSrPO_4$. The following required experimental data were used: band gap energy (~8.12 eV, see arrow 1); energy of the 4f–$5d_1$ transition of Ce^{3+} (~4.14 eV, see arrow 2) and the 5d centroid energy shift (ε_c, ~1.19 eV) of Ce^{3+} in $KSrPO_4$; the Eu^{3+}–O^{2-} charge transfer energy in $KSrPO_4$ (~4.56 eV, see arrow 3).

To construct this VRBE scheme, the Coulomb repulsion energy U, which is the energy difference between the ground state 4f-shell electron binding energies $E_{4f}(Eu^{2+})$ in Eu^{2+} and $E_{4f}(Eu^{3+})$ in Eu^{3+}, is first estimated to be about 7.09 eV from the observed Ce^{3+} 5d centroid shift ε_c (1.19 eV) using eqn (1), then the energy of the Eu^{2+} ground state $^8S_{7/2}$ in the VRBE scheme is evaluated to be −4.11 eV based on eqn (2).[20]

$$U = 5.44 + 2.834e^{-\varepsilon_c/2.2} \quad (1)$$

$$E_{4f}(Eu^{2+}) = 24.92 + \frac{18.05 - U}{0.777 - 0.0353U}. \quad (2)$$

Therefore, the Eu^{3+} ground state $^7F_0$ is about −11.20 eV in VRBE. The 4f ground state energies of other Ln^{2+} and Ln^{3+} are determined using the most recently reported energy differences of Eu^{2+}/Eu^{3+} and Ln^{2+}/Ln^{3+} in ref. 31. Then all 4f energies of Ln^{2+} and Ln^{3+} can be drawn in the VRBE scheme according to the Dieke diagram.

After we obtain the 4f ground state ($^2F_{5/2}$) energy of Ce^{3+} about −5.96 eV in the VRBE scheme, the Ce^{3+} $5d_1$ state can be derived to be approximately −1.82 eV by adding the observed energy of the 4f–$5d_1$ transition (4.14 eV, see in Fig. 3). The lowest 5d energies of other Ln^{3+} can be determined with the known energy differences of Ce^{3+} and Ln^{3+}.

The 4f–$5d_1$ transition energy of Eu^{2+} (~3.16 eV) is measured experimentally as shown in Fig. 10 or estimated from that of Ce^{3+}.[20] Hence the $5d_1$ energy of Eu^{2+} in the VRBE scheme is

determined to be −0.95 eV and the $5d_1$ energies of other Ln^{2+} are obtained from the energy differences of Eu^{2+} and Ln^{2+}.

The top of the valence band energy of $KSrPO_4$ in the VRBE scheme is estimated to be −8.67 eV by subtracting the Eu^{3+}–O^{2-} charge transfer energy (4.56 eV) from $E_{4f}(Eu^{2+})$ (−4.11 eV).[33] Subsequently, the bottom of the conduction band (CB) energy of $KSrPO_4$ in the VRBE scheme is −0.55 eV after adding the band gad energy (8.12 eV) of $KSrPO_4$.

Based on the VRBE scheme, the energy difference between the energy level of the Ce^{3+} $5d_1$ state and the bottom of the conduction band is approximately 1.27 eV. The activation energy (ΔE) of thermal quenching of Ce^{3+} 5d–4f luminescence generally corresponds to the energy required to raise an electron from the relaxed $5d_1$ excited level into the host conduction band.[34] This large energy gap explains that the luminescence of the Ce^{3+} doped $KSrPO_4$ phosphor possesses a good thermal stability.

3.4. The f–d transitions of Pr^{3+} in $KSrPO_4$

Fig. 9 shows the synchrotron radiation VUV-UV excitation spectrum of samples $K_{1.003}Sr_{0.994}Pr_{0.003}PO_4$ at 25 K with four distinct bands (A′, B′, C′, and D′). The lowest energy band is at 5.66 eV, which corresponds to the lowest 4f–5d transition of Pr^{3+}. The energy is consistent with that read from the VRBE scheme (5.64 eV). Since the CFS is almost the same for the 5d energy of Ce^{3+} as for Pr^{3+}, then the other four 4f–$5d_i$ (i = 2, 3, 4, 5) transitions of Pr^{3+} in $K_{1.003}Sr_{0.994}Pr_{0.003}PO_4$ are expected at 6.12, 6.75, 7.28, and 7.60 eV, respectively. Except for the last one (the highest $5d_5$ level), other four 5d multiplets are below the bottom of the CB. The $5d_{1-3}$ states have larger energy gaps to the bottom of the CB, and these three transitions are clearly observed in the excitation spectra.

In the inset of Fig. 9, we can find four emission bands in the range of 4.0–5.3 eV. These bands are attributed to the transitions from the lowest 5d state of Pr^{3+} terminating on $^3H_4$ (band F′: 5.27 eV), $^3H_5$ (band G′: 5.01 eV), $^3F_2$ (band I: 4.68 eV), and $^3F_4$ (band J: 4.48 eV).[35] Therefore, the Stokes shift of Pr^{3+} is approximately 0.39 eV, which coincides with that of Ce^{3+} (0.39 eV). The height-normalized VUV excitation (λ_{em} = 269 nm) and emission spectra (λ_{ex} = 213 nm) of samples $K_{1+x}Sr_{1-2x}Pr_xPO_4$ (x = 0.003, 0.007, 0.011) at 25 K are plotted in ESI Fig. S6,† showing that the f–d transitions of Pr^{3+} and Ce^{3+} have similar concentration-dependent luminescence properties including the shift of 4f–$5d_1$ excitation, the positions of zero phonon line (ZPL) and the self-absorption effect.

3.5. The redox properties of Eu in $KSrPO_4$

Fig. 10 displays the synchrotron radiation VUV-UV excitation (curve a) and laboratory UV-vis excitation (curve b) and emission spectra of sample $KSr_{0.999}Eu_{0.001}PO_4$ prepared in a CO ambiance. Considering that in the 370–470 nm range there is no Eu^{3+} emission as shown in Fig. 10(b), the excitation profile contains only weak host-related absorption in the short-wavelength range and the 4f–5d transitions of Eu^{2+} in the long-wavelength range when the emission wavelength of 422 nm is monitored. The lowest $4f^7$–$4f^6$5d excitation band in our case is about 392 nm (3.16 eV), which is empirically estimated as the energy at 15% to 20% of the maximum excitation intensity on the long-wavelength side.[36] This is close to the ZPL position (~396 nm) as shown in ESI Fig. S7.† Referring to the VRBE

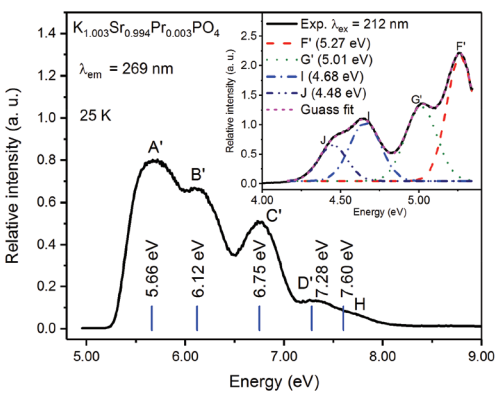

Fig. 9 Synchrotron radiation VUV-UV excitation spectrum (λ_{em} = 269 nm) of sample $K_{1.003}Sr_{0.994}Pr_{0.003}PO_4$ at 25 K; the inset shows the emission spectrum (λ_{ex} = 213 nm) at 25 K and the corresponding Gaussian fitting results.

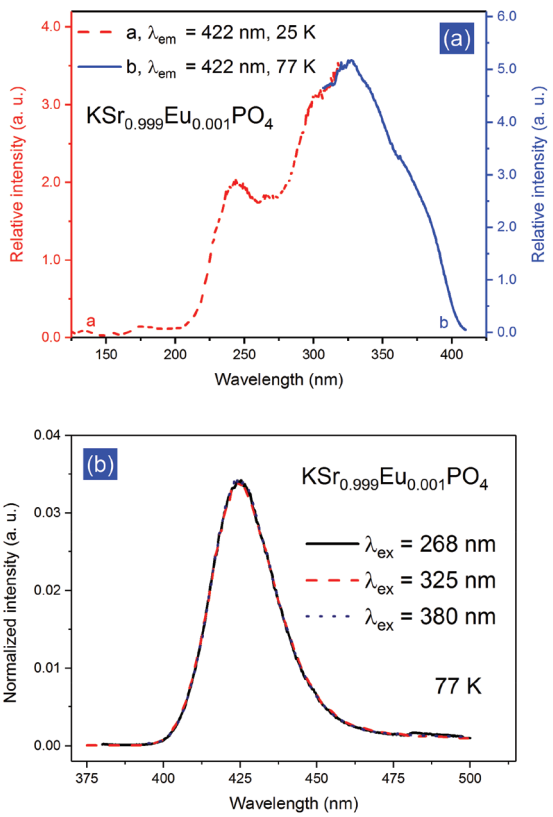

Fig. 10 (a) Synchrotron radiation VUV-UV excitation (curve a, λ_{em} = 422 nm, 25 K) and laboratory UV-vis excitation (curve b, λ_{em} = 422 nm, 77 K) spectra of sample $KSr_{0.999}Eu_{0.001}PO_4$, respectively; (b) normalized emission spectra (77 K) of the $KSr_{0.999}Eu_{0.001}PO_4$ sample prepared in a CO ambiance.

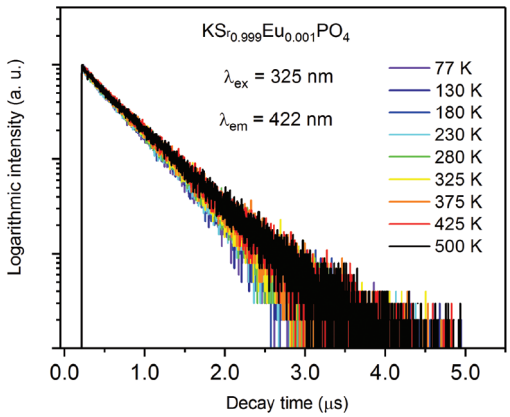

Fig. 11 Temperature dependent decay curves (λ_{ex} = 325 nm, λ_{em} = 422 nm) of the $KSr_{0.999}Eu_{0.001}PO_4$ sample prepared in a CO ambiance.

scheme (Fig. 8), the energy barrier for electrons from the excited state of Eu^{2+} to the bottom of the conduction band (ΔE) is estimated to be 0.40 eV. A small ΔE energy usually makes the Eu^{2+} emission prone to thermal quenching by means of the ionization of the 5d electrons. The large ΔE value in the present case implies a good thermal stability of luminescence of Eu^{2+} in $KSrPO_4$. The temperature-dependent decay dynamics in Fig. 11 confirms this standpoint, the thermal quenching of Eu^{2+} luminescence does not occur until 500 K.

Fig. 12 shows the emission spectra of $KSr_{0.995}Eu_{0.005}PO_4$ prepared under CO reducing, N_2 inert and air oxidizing conditions. We selected 319 nm as the excitation wavelength because both Eu^{3+} and Eu^{2+} absorb at this wavelength [see Fig. 6 and 10(a)]. In Fig. 12, the broad band at 425 nm belongs to d–f emission of Eu^{2+} and several sharp lines in the long-wavelength range correspond to Eu^{3+} f–f emission. Apparently, Eu^{3+} can be reduced to Eu^{2+} under CO reducing, N_2 inert, and air oxidizing conditions, but the reduction degrees are different. To express the degree of reduction of Eu^{3+} under these conditions, we calculated the ratios (A_2/A_3) of the integrated area of emission between 380 and 450 (A_2) and between 550 and 730 (A_3) nm, respectively. The results are 99.8/0.02 (CO), 46.4/53.6 (N_2), 31.9/68.1 (air), implying that the reduction degree decreases from CO to N_2 and air. When prepared under CO conditions, it dominantly displays Eu^{2+} emission, and Eu^{3+} emission is very weak. For further demonstration, under excitation of the charge transfer band of Eu^{3+} (272 nm), the emission spectra of representative $KSr_{1-x}Eu_xPO_4$ (x = 0.001, 0.009 and 0.015) samples annealing under CO condition are shown in ESI Fig. S8,† indicating that Eu^{2+} ions are dominant. Under N_2 and air conditions, Eu^{2+} emission dramatically decreases but is still present, showing that Eu^{3+} is partially reduced to Eu^{2+}, and it seems that more Eu^{3+} ions are reduced to Eu^{2+} when prepared under N_2 conditions.

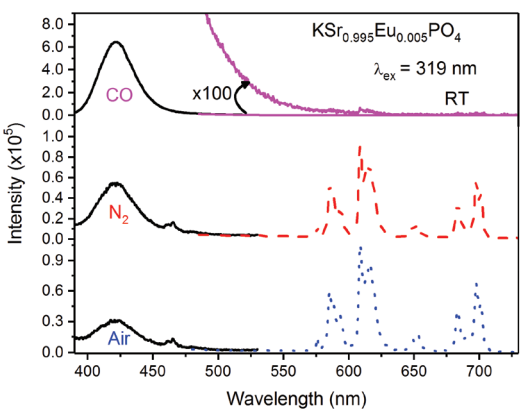

Fig. 12 Emission spectra (λ_{ex} = 319 nm) of $KSr_{0.995}Eu_{0.005}PO_4$ samples synthesized under CO (top), N_2 (middle) and air (bottom) conditions.

The redox behaviour of Eu in $KSr_{0.995}Eu_{0.005}PO_4$ can be understood with the VRBE scheme in Fig. 8 when we consider that the redox properties of Eu ions are related to the Fermi energy position. The Fermi energy level locates midway the bottom of the CB and the top of the valence band (VB) when the phosphor is synthesized under an inert atmosphere or near −4.06 eV (black dot curve) in the VRBE scheme. Eu ions usually prefer the divalent state when the ground state of Eu^{2+} is near or below the Fermi energy, and becomes more stable when it is further below the Fermi energy level. Referring to the VRBE scheme, it is almost the same as the Fermi energy level for the $KSr_{0.995}Eu_{0.005}PO_4$ sample annealed in N_2, so Eu^{3+} can be partially reduced to Eu^{2+} in N_2. The Fermi energy position somewhat increases or decreases under oxidizing or reducing conditions in comparison with that under inert conditions. As a result, the reduction degree of Eu^{3+} increases under CO reducing condition but decreases under air oxidizing condition. On the other hand, when we consider the structure of the host compound, the stabilization of Eu^{2+} would relate to the similar ionic radii of Sr^{2+} and Eu^{2+}, and the rigid tetrahedral three-dimensional PO_4^{3+} groups as previously commented.[5,37]

4. Conclusions

We investigated the synchrotron radiation VUV-UV excitation spectra and the corresponding emission spectra of Ln-doped $KSrPO_4$ (Ln = Ce^{3+}, Eu^{3+}, Eu^{2+}, Pr^{3+}) phosphors prepared by a high-temperature solid-state reaction method. It is found that five 4f–5d transitions of Ce^{3+} are at ~4.14, 4.60, 5.23, 5.76 and 6.08 eV, respectively. The energy of the Eu^{3+}–O^{2-} charge transfer state is found at 4.56 eV (272 nm), and the mobility band gap of $KSrPO_4$ is estimated to be 8.12 eV. Accordingly, the VRBE scheme is constructed and applied to understand the excellent thermally stable luminescence of Ce^{3+} and Eu^{2+}, 4f–5d transitions of Pr^{3+}, and the redox properties of $Eu^{2+/3+}$.

The energy differences between the lowest 5d states of Ce^{3+}/Eu^{2+} and the bottom of the conduction band are read about 1.27/0.40 eV from the VRBE scheme, individually. Referring to the experimental data and derived energy barriers, the 5d–4f luminescence of Ce^{3+} and Eu^{2+} has a good thermal stability and the thermal quenching does not occur as far as 500 K. In

terms of the VRBE scheme, the lowest 5d energy of Pr^{3+} is evaluated to be about 5.64 eV, which is in good line with the experimental observation (5.66 eV), and other four 5d orbitals of Pr^{3+} are with energies approximately 6.12, 6.75, 7.28, and 7.60 eV, respectively. Eu^{3+} can be reduced to Eu^{2+} under CO reducing, N_2 inert, and air oxidizing conditions, respectively. The reduction is almost complete in a CO reducing ambiance, while that is partial under N_2 inert and air oxidizing conditions. From the viewpoint of the host structure, the similar ionic radii of Sr^{2+} and Eu^{2+}, and the rigid tetrahedral three-dimensional PO_4^{3+} groups may be responsible for this phenomenon. From the standpoint of energy, this may relate to nearly the same energies of the Eu^{2+} ground state and the Fermi level of $KSrPO_4$ under neutral conditions.

Conflicts of interest

There are no conflicts to declare.

Acknowledgements

This work has been financially supported by the National Natural Science Foundation of China (U1432249, U1632101 and 21671201) and the Science and Technology Project of Guangdong Province (2017A010103034).

Notes and references

1 N. Guo, H. P. You, C. Z. Jia, R. Z. Ouyang and D. H. Wu, *Dalton Trans.*, 2014, **43**, 12373.
2 Z. P. Ci, M. D. Que, Y. R. Shi, G. Zhu and Y. H. Wang, *Inorg. Chem.*, 2014, **53**, 2195.
3 X. Chen, Z. G. Xia and Q. L. Liu, *Dalton Trans.*, 2014, **43**, 13370.
4 W. G. Xiao, D. Wu, L. L. Zhang, X. Zhang, Z. D. Hao, G. H. Pan, L. G. Zhang, X. W. Ba and J. H. Zhang, *Inorg. Chem.*, 2017, **56**, 9938.
5 M. Y. Peng, Z. W. Pei, G. Y. Hong and Q. Su, *J. Mater. Chem.*, 2003, **13**, 1202.
6 M. Y. Peng, Z. W. Pei, G. Y. Hong and Q. Su, *Chem. Phys. Lett.*, 2003, **371**, 1.
7 P. Dorenbos, *Chem. Mater.*, 2005, **17**, 6452.
8 A. Bessiere, P. Dorenbos, C. Eijk, K. Krämer, H. Güdel, C. Donega and A. Meijerink, *Nucl. Instrum. Methods Phys. Res., Sect. A*, 2005, **537**, 22.
9 M. Alekhin, J. Haas, I. Khodyuk, K. Krämer, P. Menge, V. Ouspenski and P. Dorenbos, *Appl. Phys. Lett.*, 2013, **102**, 161915.
10 Y. T. Wu, L. Boatner, A. Lindsey, M. Zhuravleva, S. Jones, J. Auxier, H. Hall and C. Melcher, *Cryst. Growth Des.*, 2015, **15**, 3929.
11 W. J. Zhou, D. J. Hou, F. J. Pan, B. B. Zhang, P. Dorenbos, Y. Huang, Y. Tao and H. B. Liang, *J. Mater. Chem. C*, 2015, **3**, 9161.
12 Y. H. Wang, M. G. Brik, P. Dorenbos, Y. Huang, Y. Tao and H. B. Liang, *J. Phys. Chem. C*, 2014, **118**, 7002.
13 Y. S. Tang, S. F. Hu, C. C. Lin, N. Bagkar and R. S. Liu, *Appl. Phys. Lett.*, 2007, **90**, 151108.
14 C. C. Lin, R. S. Liu, Y. S. Tang and S. F. Hu, *J. Electrochem. Soc.*, 2008, **155**, J248.
15 Y. M. Peng, Y. K. Su and R. Y. Yang, *Opt. Mater.*, 2013, **35**, 2102.
16 A. A. Coelho, *TOPAS Academic, Version 4*, Coelho Software, Brisbane, Australia, 2005.
17 H. H. Lin, D. J. Hou, L. Li and H. B. Liang, *Dalton Trans.*, 2013, **42**, 12891.
18 Z. Xia and Q. Liu, *Prog. Mater. Sci.*, 2016, **84**, 59.
19 Z. Xia, Z. Xu, M. Chen and Q. Liu, *Dalton Trans.*, 2016, **45**, 11214.
20 R. D. Shannon, *Acta Crystallogr., Sect. A: Cryst. Phys., Diffr., Theor. Gen. Crystallogr.*, 1976, **A32**, 751.
21 P. Dorenbos, *J. Lumin.*, 2013, **135**, 93.
22 C. H. Huang, T. M. Chen and B. M. Cheng, *Inorg. Chem.*, 2011, **50**, 6552.
23 L. Pieterson, M. Reid, R. Wegh, S. Soverna and A. Meijerink, *Phys. Rev. B: Condens. Matter Mater. Phys.*, 2002, **65**, 045113.
24 H. B. Liang, J. Wang, X. Ye, Z. F. Tian, H. H. Lin, Q. Su, Y. Tao, J. H. Xu, Y. Huang, G. B. Zhang and Y. B. Fu, *J. Alloys Compd.*, 2006, **425**, 307.
25 H. B. Liang, H. H. Lin, G. B. Zhang, P. Dorenbos and Q. Su, *J. Lumin.*, 2011, **131**, 194.
26 R. Shi, M. M. Qi, L. X. Ning, F. J. Pang, L. Zhou, W. J. Zhou, Y. C. Huang and H. B. Liang, *J. Phys. Chem. C*, 2015, **119**, 19326.
27 Y. H. Wang, J. H. Zhang, D. J. Hou, H. B. Liang, P. Dorenbos, S. Sun and Y. Tao, *Opt. Mater.*, 2012, **34**, 1214.
28 Z. W. Zhang, J. W. Hou, J. Li, X. Y. Wang, X. Y. Zhu, H. X. Qi, R. Lv and D. J. Wang, *J. Alloys Compd.*, 2016, **682**, 557.
29 Q. Peng, C. M. Liu, D. J. Hou, W. J. Zhou, C. G. Ma, G. K. Liu, G. M. Brik, Y. Tao and H. B. Liang, *J. Phys. Chem. C*, 2016, **120**, 569.
30 V. Bachmann, C. Ronda and A. Meijerink, *Chem. Mater.*, 2009, **21**, 2077.
31 P. Dorenbos, *Opt. Mater.*, 2017, **69**, 8.
32 O. L. Malta, W. M. Azevedo, E. A. Gouveia and G. F. De Sá, *J. Lumin.*, 1982, **26**, 337.
33 P. Dorenbos, *J. Lumin.*, 2005, **111**, 89.
34 J. Ueda, S. Tanabe and T. Nakanishi, *J. Appl. Phys.*, 2011, **110**, 053102.
35 E. Kolk, P. Dorenbos, A. Vink, R. Perego and C. Eijk, *Phys. Rev. B: Condens. Matter Mater. Phys.*, 2001, **64**, 195129.
36 P. Dorenbos, *J. Phys.: Condens. Matter*, 2003, **15**, 575.
37 Z. W. Pei, Q. H. Zeng and Q. Su, *J. Phys. Chem. Solids*, 2000, **61**, 9.